PAPER

An integrated microfluidic platform for selective and real-time detection of thrombin biomarkers using a graphene FET†

Niazul I. Khan,[a] Mohammad Mousazadehkasin,[b] Sujoy Ghosh,[a,c] John G. Tsavalas[b,c,d] and Edward Song ✶[a,c,d]

Lab-on-a-chip technology offers an ideal platform for low-cost, reliable, and easy-to-use diagnostics of key biomarkers needed for early screening of diseases and other health concerns. In this work, a graphene field-effect transistor (GFET) functionalized with target-binding aptamers is used as a biosensor for the detection of thrombin protein biomarker. Furthermore, this GFET is integrated with a microfluidic device for enhanced sensing performances in terms of detection limit, sensitivity, and continuous monitoring. Under this platform, a picomolar limit of detection was achieved for measuring thrombin; in our experiment measured as low as 2.6 pM. FTIR, Raman and UV-Vis spectroscopy measurements were performed to confirm the device functionalization steps. Based on the concentration-dependent calibration curve, a dissociation constant of K_D = 375.8 pM was obtained. Continuous real-time measurements were also conducted under a constant gate voltage (V_{GS}) to observe the transient response of the sensor when analyte was introduced to the device. The target selectivity of the sensor platform was evaluated and confirmed by challenging the GFET biosensor with various concentrations of lysozyme protein. The results suggest that this device technology has the potential to be used as a general diagnostic platform for measuring clinically relevant biomarkers for point-of-care applications.

1 Introduction

Graphene, a 2D material of one atomic layer thickness, shows a plethora of interesting properties,[1–8] such as high carrier mobility, large specific surface area, excellent electrical conductivity, planar structure, biocompatibility, high stability and flexibility. As a result, graphene materials have been used in many electronic applications including photodetectors,[2,6] capacitors[8] as well as biosensors.[3] Specifically, the utilization of graphene as a conduction channel in a field-effect transistor (FET) has been shown by us and others to have potential for sensitive biodetection.[3,4,9] To date, there exist many different detection principles in biosensors such as electrochemical impedance spectroscopy,[10–12] high-performance liquid chromatography (HPLC),[13] quartz crystal microbalance (QCM),[14,15] surface plasmon resonance (SPR),[16] and fluorescence based optical detection[17,18] to name a few. However, there are some limitations with these techniques such as tedious sample preparation as well as sophisticated and expensive instrumentation with consistent need for trained operators. By contrast, FET-based detection offers a variety of advantages such as high sensitivity, fast detection time, easy integration with the integrated circuit (IC) manufacturing process, miniaturization, low-cost, continuous real-time sensing and label-free detection.[19–21]

A graphene FET (GFET) biosensor works either by the electrostatic gating effect or direct charge transfer to graphene, also known as the doping effect, or a combination of both.[22,23] The electrostatic gating effect dominates when the concentration of charged molecules near the graphene surface is high and the distance between those molecules and graphene is within the Debye screening length so that the adsorbed biomolecules collectively act as an effective gate voltage. Any additional charged molecules adsorbed on graphene surface causes a change in this external electric field that modulates the drain–source current. By contrast, the doping effect is caused by the direct charge transfer from the adsorbed molecules to graphene channel specially when the adsorbed

[a]Department of Electrical and Computer Engineering, University of New Hampshire, Durham, NH 03824, USA. E-mail: edward.song@unh.edu
[b]Department of Chemistry, University of New Hampshire, Durham, NH 03824, USA
[c]Center for Advanced Materials and Manufacturing Innovation, University of New Hampshire, Durham, NH 03824, USA
[d]Materials Science Program, Demeritt Hall, University of New Hampshire, Durham, NH 03824, USA
†Electronic supplementary information (ESI) available. See DOI: 10.1039/D0AN00251H

species are at low concentration or weekly charged. In this case, the adsorption density is quite small and the distance between the adsorbed molecules is larger than the Debye length of the channel material and the charge transfer is dominant between the adsorbed species and the channel material.[23–26] The competition between the doping effect and the gating effect determines the appropriate sensing response. For example, if the doping effect is dominant, the current increases in a p-type semiconducting channel; whereas if the gating effect is dominant, the conduction current decreases.[23] This change in the drain current can be utilized as an interrogation strategy to probe the adsorbed biomolecules. Moreover, the ambipolar transfer (drain current *vs.* gate voltage) curve of the GFET devices provides an additional sensing mechanism by measuring the surface charge-induced shift in the Dirac voltage (ΔV_{Dirac}) which is defined as the gate voltage at minimum drain current. Hence, the GFET as a biosensing platform has been applied for the detection of various target analytes including antigens, antibodies and charged molecules.[9,22,27–31]

Thrombin is an important protein biomarker for a number of diseases as it plays a central role in several cardiovascular diseases and the regulation of tumor growth. It is also responsible for thrombosis and platelet activation and therefore, is involved in many processes such as inflammation and tissue repair at the blood vessel wall.[32] Hence, the selective and sensitive detection of thrombin will be useful in surgical procedures and cardiovascular disease therapy. Moreover, thrombin is positively charged[33,34] at neutral pH enabling it to be detected on a graphene-based sensing platform. Existing thrombin biosensors commonly use either antibodies or aptamers as the target capture probe to enhance selectivity. Recently, aptamers have become a popular choice of target receptors due to a number of advantages they offer compared to antibodies including shorter length and simpler structure, lower cost, higher stability in harsh environmental conditions, longer shelf-life and mass-producibility. Moreover, they can be selected *in vitro* with high affinity for a wide range of analytes ranging from proteins, peptides, amino acids, drugs, metal ions and to even whole cells.[35]

Although GFET-based biosensors have been frequently reported,[9,36,37] when it comes to analyte liquid control, a small volume of sample droplet is often placed over the graphene surface to form a liquid gate which is exposed to the open atmosphere. This type of sensing arrangement makes the sample loading and disposal difficult to control and also makes the device vulnerable to external disturbances such as evaporation. These factors could lead to inaccurate measurements and poor sensing performances. Furthermore, measurements taken during static flow (non-moving fluid) may lead to the mass-transfer limitation in the kinetic binding processes.[38] Therefore, in efforts to address such challenges, the integration of the GFET device with a microfluidic system is implemented.

The integration of microfluidics to biosensors has emerged as a promising approach in biomedical applications as microfluidics offer numerous advantages over traditional assays. Conceptually, microfluidics is the manipulation of fluids in submillimeter length scale with technologies first developed by the semiconductor industry and later expanded by the micro-electromechanical systems (MEMS) field. Commonly known as miniaturized Total Analysis System (μTAS) or Lab-on-a-Chip (LoC) technologies, microfluidic technologies have been applied to biomedical research in order to (1) streamline complex assay protocols, (2) to reduce the sample volume and detection time substantially, (3) to reduce the cost of reagents while maximizing the information collected, (4) to enable automated measurement with high throughput, (5) to potentially enhance the sensitivity by increasing surface-to-volume ratio, and (6) to enable portability, disposability and real-time detection.[39–41] Moreover, integration to microfluidic channels improves the accuracy of measurements by preventing evaporation of buffer solution.[42] To exploit these advantages of the microfluidic technology, the integration of GFET biosensors and microfluidics has been proposed by several research groups. For example, Islam *et al.* (2019) have developed a microfluidic GFET biosensor for femtomolar detection of chlorpyrifos.[28] Yang *et al.* (2015) have built a microfluidic aptasensor that combines aptamer-based selective analyte enrichment, isocratic elution with GFET-based nanosensing for sensitive and label-free detection of small biomolecules.[43] Saltzgaber *et al.* (2013) have demonstrated a large-scale GFET fabrication using a CVD-grown graphene layer and the detection of thrombin biomarkers.[44] Therefore, GFET-based thrombin sensing has the potential to be used as a point-of-care diagnostic device. However, for this to be used reliably in a real-world setting, the GFET must achieve the limit of detection, sensitivity, and analyte selectivity required for clinical use. As an example, thrombin concentration in blood can change from picomolar to micromolar range depending on the health condition. Therefore, a thrombin biosensor must exhibit a limit of detection in the picomolar level as well as a detection range up to a micromolar concentration.[45]

In this work, we demonstrate that the aptamer-modified microfluidic GFET platform can selectively detect the thrombin biomarker with a detection limit in the picomolar range. Detailed analyses of the sensing performances as well as device characterization, including aptamer packing density and continuous real-time sensing, are presented. The GFET was fabricated using the CVD-grown graphene transferred on prefabricated gold electrodes. Contrary to the commonly used out-of-plane gate electrode,[31] an in-plane gate electrode was used here to control the gate–source voltage of the GFET. This in-plane gate electrode fabricated at the same lithography step as the source and the drain electrodes reduces the processing steps in device fabrication as well as enables the intended miniaturization of the microfluidic platform. Furthermore, although the mechanical exfoliation technique may yield higher quality of graphene, the CVD-based graphene allows large-scale production of graphene with controllable sensing area.[1,46] Then, the GFET module was integrated with a microfluidic chip to build a miniaturized and portable biosensing

module. The detection was performed by measuring the change in the Dirac voltage (ΔV_{Dirac}) as well as by measuring the change in the drain–source current continuously in real-time to observe the transient behavior during constant sample flow mode. Our biosensor was able to detect thrombin with a concentration as low as 2.6 pM ($\approx$260 NIH microunits per mL), which is significantly lower than previously reported values.[47,48] The binding affinity between the aptamer and the thrombin was quantified by calculating the dissociation constant which was confirmed by transient measurements in real-time.

2   The principle of operation of the microfluidic GFET-based biosensor platform

The working principle of the microfluidic thrombin biosensor is illustrated in Fig. 1. Fig. 1A shows the schematic view of the integrated GFET device where a microfluidic channel with an inlet and an outlet traverses the source, drain and an in-plane gate electrode. Fig. 1B depicts the three-electrode transistor device setup where the FET measurements were performed by applying a constant drain voltage (V_{DS}) between the source and the drain, whereas a varying voltage (V_{GS}) was applied on the gate. Fig. 1C shows the mechanism by which target binding and detection is achieved. The Dirac voltage shifts either to the left or right depending on the type and concentration of the adsorbed charged species. If the adsorbed species are at low concentration or weekly charged, doping effect dominates while gating effect becomes dominant at high concentration or strongly charged species.[22,23] In our experiments, while thrombin, which has an isoelectric point of around 9.5, was weekly and positively charged at pH 7.4,[33,34] p-type doping was generated in graphene upon binding to the thrombin aptamer.

This p-type doping causes the Dirac voltage to shift in the positive direction.[31] By monitoring the shift in the Dirac voltage, the presence of thrombin can be measured quantitatively.

3   Materials and methods

3.1   Materials

The aminated anti-thrombin DNA aptamers and the aminated anti-lysozyme aptamers (for control experiments detailed in the ESI†) were purchased from Sigma-Aldrich. The aptamers were amine-terminated with the following sequences:

Anti-thrombin: 5′-NH_2-$(CH_2)_6$-CCA TCT CCA CTT GGT TGG TGT GGT TGG-3′.[48]

Anti-lysozyme: 5′-NH_2-$(CH_2)_6$-ATC AGG GCT AAA GAG TGC AGA GTT ACT TAG-3′.[49]

Thrombin from human plasma was also purchased from Sigma-Aldrich. The protein stock solutions were prepared by dissolving the lyophilites in deionized water to achieve the different molar concentrations needed for the experiment and were stored at 4 °C. The diluted solutions for sensing experiments were prepared by adding 0.01× PBS (pH: 7.4) to the stock solution. Since GFETs can only observe changes in the charge density that occurs within the distance similar to the Debye length from the graphene surface, it is critical to ensure that the Debye length be sufficiently large. For an effective GFET-based sensing, the Debye length should theoretically be comparable to the aptamer length.[31] In this work, the estimated length of the anti-thrombin aptamer is approximately 9.1 nm. While 1× PBS has a Debye length of 0.7 nm, the Debye length for 0.01× PBS is 7.3 nm.[31,50] For this reason, 0.01× PBS was chosen as a running buffer for the electrical measurements. The CVD-grown graphene sheets were purchased from Graphenea Inc. as easy transfer monolayer graphene on a polymer film.
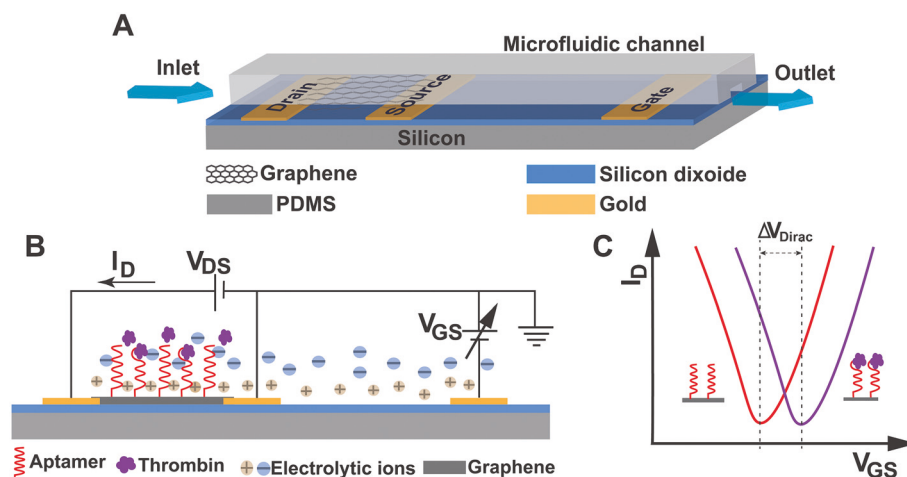

Fig. 1 Conceptual illustration of the microfluidic GFET biosensor: (A) schematic illustration of the integrated device; (B) GFET device setup with drain, source and gate electrodes; and (C) the sensing mechanism based on surface charge-induced Dirac voltage shift (ΔV_{Dirac}) in the GFET $I_{\text{D}}-V_{\text{GS}}$ transfer characteristics curve.

3.2 Device fabrication, surface functionalization, and measurement methods

3.2.1 Device fabrication. For the fabrication of the FET devices, gold electrodes for the source, drain and gate contacts were patterned on a SiO$_2$/Si substrate using conventional microfabrication techniques. Briefly, chromium (Cr, 5 nm) and gold (Au, 60 nm) films were thermally evaporated onto the substrate. Then the source, drain and gate contact regions were formed by standard photolithography, followed by wet chemical etching of Cr/Au layers. The Cr layer was used as an adhesion promoter between Au and SiO$_2$. After the electrode fabrication, a 5 mm × 5 mm graphene film was transferred onto the electrodes (see ESI† for details).

The microfluidic channel with a dimension of 30 mm × 600 µm × 100 µm was fabricated with a polydimethylsiloxane (PDMS) block using the cast molding technique.[51] The inlet and the outlet of the channel were formed with metal tubing and the PDMS block was securely clamped to the GFET device. A photograph of the final integrated GFET module is shown in Fig. 2A. The inlet and outlet of the device were connected with silicone tubes for analyte injection and removal. A motorized syringe pump (Harvard apparatus) was used for driving the analyte solutions from syringes. Such a setup enables stable flow of the analyte solution and minimizes noise induced by liquid loading processes, as required for real-time, precise measurement of kinetic processes for aptamer–protein binding interaction.

The module consists of two GFET arrays, each array containing 3 GFET devices formed by 4 equally spaced (50 µm gap) gold electrodes (100 µm wide) with two adjacent electrodes acting as the source and the drain. For the 3 GFET devices in each array, one in-plane gold electrode (approximately 6.0 mm

spaced apart from the 4 electrodes) serves as the gate. Table S1† summarizes the labeling of the 6 GFET devices in the module.

3.2.2 Surface functionalization. Prior to using the GFET devices as biosensors, the graphene surface was functionalized in several steps as shown in Fig. 2B. First, the graphene was treated with 10 mM 1-pyrene butyric acid N-hydroxysuccinimide ester (PBASE) solution in dimethyl formamide (DMF) delivered *via* the microfluidic flow system for 12 hours. The PBASE molecules were non-covalently coupled to the graphene surface by π–π stacking interactions between complementary aromatic rings in the graphene and the pyrene functional group of PBASE.[52] The microfluidic channel was then rinsed by flowing DMF, ethanol and DI water sequentially to remove any unbound PBASE. Next, aptamers were introduced into the channel by flowing a 2 µM aminated (at the 5′-end) target specific aptamer solution and 0.1% (v/v) triethylamine (TEA) for a duration of 12 hours. The aptamers were covalently grafted to the surface bound PBASE molecules *via* amide bond formation resulting from reaction with the primary amine on the probe aptamer.[42,53] Successful coupling of PBASE to graphene and aptamer to PBASE was confirmed by Raman, FTIR and UV-Vis analyses.

3.2.3 Electrical measurements. All electrical measurements were performed on a Micromanipulator (450 PM-B) probe station using a PC-based LabVIEW program. A Keysight precision source/measure unit (B2902A) was used for biasing as well as for supplying input voltages and measuring the output currents. The drain–source voltage was maintained at 250 mV for all I_D–V_{GS} transfer curve measurements. The liquid–gate voltage was linearly scanned from 0 V to 2.5 V with a voltage step of 12.5 mV using the gate electrode. During each step, the V_{GS} value was maintained for 1 second to stabilize I_D to ensure reliability of I_D–V_{GS} transfer curves resulting a scan rate of 12.5 mV s^{-1}. All the measurements were performed with a
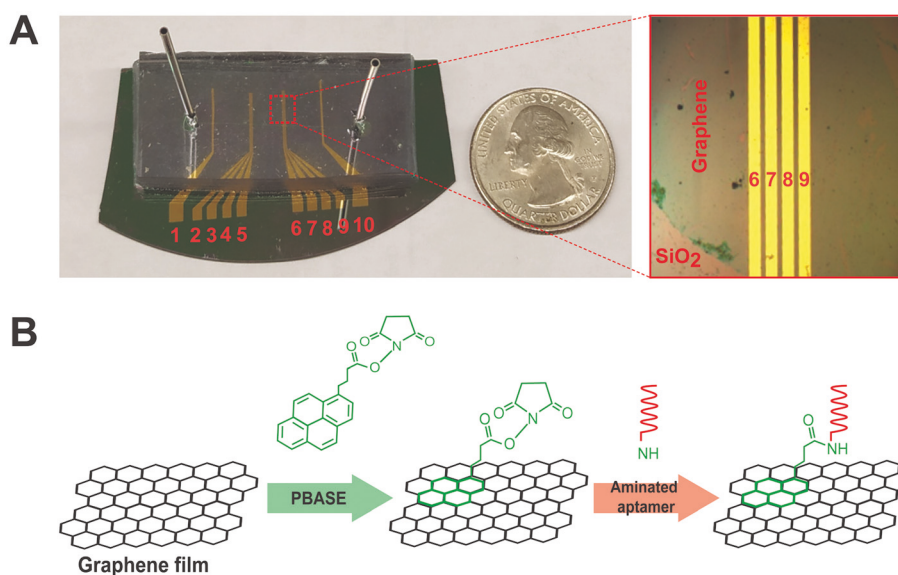

Fig. 2 Device fabrication and graphene functionalization steps: (A) photograph of the microfluidic-integrated GFET module (left) and the enlarged view of the source–drain electrodes of the right GFET array (right); and (B) schematic illustration of the surface functional steps applied to the GFET devices before using it as sensors.

fluid flow rate of 20 μl min⁻¹. To evaluate the electrochemical effects on the GFET devices, the leakage current at the gate electrode was also measured. The leakage current I_{GS} remained less than 1 μA and thus was considered negligible, as the magnitude of the I_D was in the range of 800 μA.

For the transient measurements of real-time monitoring of the aptamer–protein association and dissociation, I_D was measured by keeping $V_{DS} = 0.1$ V. The gate source voltage (V_{GS}) was also fixed at a voltage near the charge neutrality point (*i.e.* V_{Dirac}) such that it locates in the linear region of the I_D–V_{GS} transfer curve yielding a high value of transconductance, g_m (see ESI Fig. S2†). Here, the data points were collected once per second. Various concentrations of thrombin were injected at a flow rate of 20 μl min⁻¹ for 1 hour. Afterward, a 0.01× PBS buffer was flowed for another hour to dissociate and remove the bound protein biomarkers.

4 Experimental results and discussion

4.1 Characterization of the surface functionalization

The interaction between PBASE and graphene *via* π–π stacking was characterized by Raman spectroscopy. For the sample preparation, the GFET device was functionalized with 10 mM PBASE in dimethyl formamide (DMF) for 2 hours followed by washing with DMF, ethanol and DI water. The Raman spectra for both the bare graphene and the PBASE-treated graphene are presented in Fig. 3A. The G- and 2D-bands in the spectra indicate the presence of graphene.[54] Moreover, the peak at 1618 cm⁻¹ which is attributed to the pyrene group resonance peak due to the π–π stacking interaction[22,31] between the aromatic rings of the pyrene group of PBASE and the basal plane of graphene which confirms the coupling of PBASE to graphene.

To characterize the crosslinking of aminated aptamers with PBASE, both the aptamers and PBASE were reacted in a 3 : 2 mixture of tetrahydrofuran (THF) and PBS buffer. The aptamer-grafted PBASE was purified by column chromatography and was allowed to dry in an oven at 45 °C for 8 h. The FTIR spectra of both dried PBASE-aptamer and pure PBASE powder are presented in Fig. 3B where the presence of a strong peak at 1653 cm⁻¹ (C=O stretching in the amide I) and the broad stretching vibration peak around 3300–3550 cm⁻¹ (N–H from the amide, O–H solely on the DNA) confirm the amide bond formation.[55] By contrast, the corresponding peak for C=O in PBASE appears at 1725 cm⁻¹ and the absorption peaks at 1785 cm⁻¹ and 1816 cm⁻¹ are related to the sym-
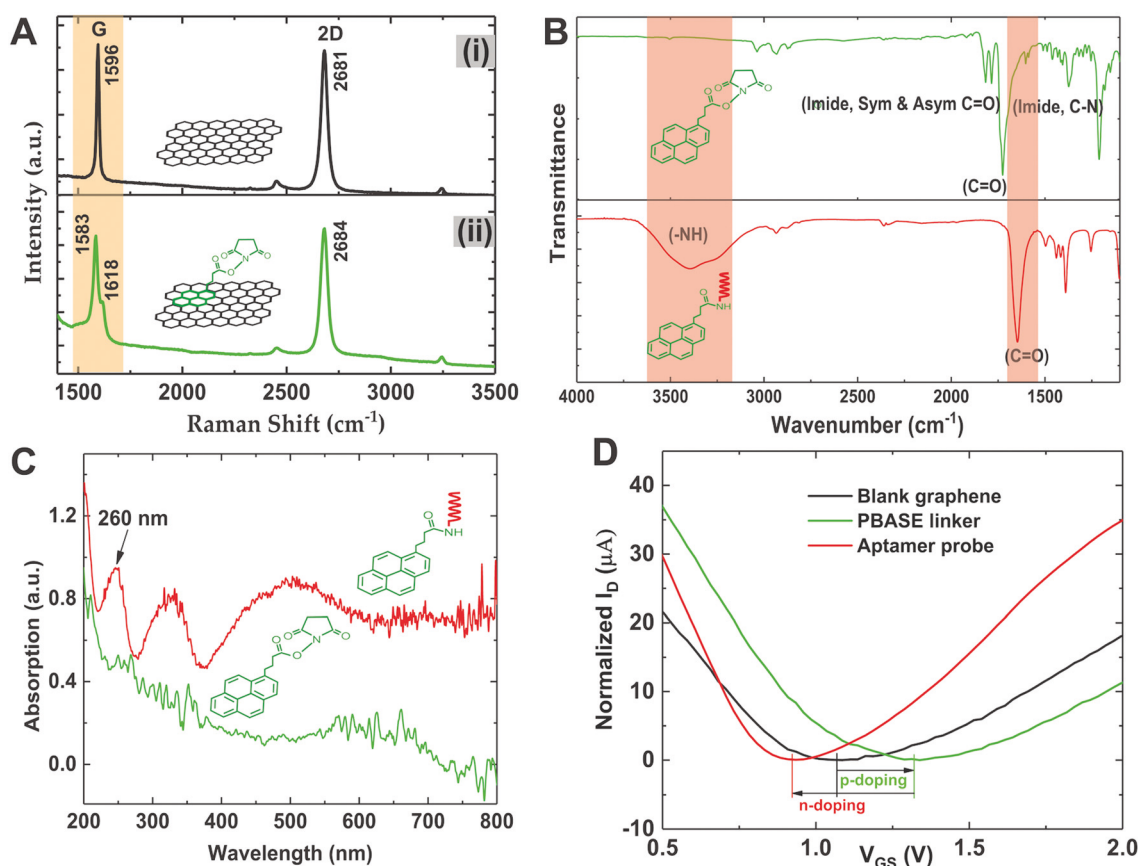

Fig. 3 Characterization of linking of aptamer to GFET: (A) Raman spectrum (excitation by 532 nm) showing the coupling of PBASE to graphene; (B) FTIR spectrum showing the covalent binding of aminated aptamer with PBASE; (C) UV-visible spectrum showing the final aptamer crosslinking to PBASE/graphene; and (D) I_D–V_{GS} transfer characteristics showing the effects of surface functionalization of the graphene.

metric and asymmetric stretching vibration of the two C=O groups in the imide, while the stretching peak for C–N in the imide appears at 1375 cm^{-1}.

After the PBASE and aptamer crosslinking was confirmed, the PBASE functionalized GFET device was exposed to a 2 μM aminated (at the 5′ end) target specific aptamer solution for 12 hours. The sample was then washed with DI water and dried followed by UV-Vis spectroscopy measurements. The UV-Vis absorption spectroscopy is shown in Fig. 3C where the absorption peak at around λ = 260 nm is a characteristic peak of the DNA oligonucleotides. This proves successful immobilization of the aptamer receptor in the graphene channel.

We further investigated the functionalization-induced doping by measuring the I_D–V_{GS} transfer curves of the microfluidic-GFET device before and after PBASE coupling. As can be seen from Fig. 3D, immobilizing PBASE linker to graphene causes the Dirac voltage to shift right. This shift in the positive direction can be explained by the p-type doping effect due to the charge transfer between PBASE and graphene.[22,31] It is important to note that while the pyrene group of PBASE is electron-rich and not expected to induce p-type doping to the graphene, the carbonyl group of PBASE is an electron-withdrawing group that can cause electron transfer from graphene to the linker molecule.[42,56] After PBASE functionalization, the devices were further modified with DNA-based aptamer which caused the Dirac voltage to shift left with respect to the position after the PBASE modification step. This is due to the n-type doping of graphene channel by the electron rich nucleotide bases of the DNA aptamers acting as electron donors when interacting with graphene.[24,57] Using the shift in Dirac voltage, the aptamer density was estimated to be 1.427×10^{11} cm^{-2} which is equivalent to 26.5 nm aptamer probe spacing (see the ESI† for the detailed calculation).

4.2 The FET-based sensing experiments

4.2.1 Control experiments. To examine the inertness of the bare graphene to thrombin, a set of control experiments were performed by exposing bare graphene to thrombin solution of various concentrations. As shown in Fig. S1(A) in the ESI,† no significant shift in the Dirac voltage is observed indicating non-responsive behavior of the bare unmodified graphene to thrombin. We also performed another set of control experiments to examine the adsorption behavior of thrombin on GFET device modified with a different aptamer sequence. In this case, the graphene was modified with anti-lysozyme aptamers and were exposed to different concentrations of thrombin solutions. The measured transfer curves are presented in Fig. S1(B)† which shows that there is no significant shift in the Dirac voltage, indicating negligible non-specific adsorption of thrombin protein during the sample flow.

4.2.2 The effects of analyte concentration on the Dirac voltage shift. Following the functionalization and aptamer immobilization, the GFET devices were exposed to different concentrations of thrombin by delivering them through the microfluidic channel at 20 μl min^{-1} for 45 minutes each. Each sample exposure was followed by a washing step with 0.01×

PBS buffer for another 45 minutes for sensor regeneration. Fig. 4A shows the I_D–V_{GS} characteristics of the developed biosensor after exposure to different concentrations of thrombin protein. Exposure to 1 pM of thrombin caused a Dirac voltage shift (ΔV_{Dirac}) of 101 mV in the positive direction with respect to V_{Dirac} = 934.4 mV at 0 pM thrombin. With increasing concentrations of the thrombin biomarker, V_{Dirac} continues to shift further to the right until it begins to saturate at approximately 100 nM. This result is consistent with the cationic nature of thrombin protein at neutral pH.[33,34] Upon binding of the thrombin to the anti-thrombin aptamer, the net positive charge of the protein causes p-type doping of the graphene which explains the right-shift of the Dirac voltage.[9] Fig. 4B depicts the concentration dependent calibration curve obtained by plotting the Dirac voltage shift (ΔV_{Dirac}) relative to the zero concentration of the analyte (0 pM Thr). As indicated by the error bars in Fig. 4B, fabricating reproducible GFET devices is a challenge. This is primarily due to the variations in the graphene sheet in terms of the graphene channel area as well as the defects and grain boundaries which can all have a significant impact on the electronic properties of the film. However, the device reproducibility can be improved by directly growing and patterning the graphene on the substrate rather than transferring the film manually.

The calibration curve profile is best fitted by a model adapted from the Hill–Langmuir equation that describes the equilibrium binding of a ligand by a receptor:[58–60]

$$\Delta V_{Dirac} = \frac{V_0 + V_m \left(\frac{x}{K_D}\right)^n}{1 + \left(\frac{x}{K_D}\right)^n}$$

where V_0 is the estimated minimum response with all binding sites empty, V_m is the estimated maximum response with all the binding sites occupied, x is the target concentration, K_D is the effective dissociation constant that represents the concentration at which half of the available binding sites are occupied, and n represents the Hill coefficient.

The best fit (R^2 = 0.9925) values are summarized in Table 1 where the Hill coefficient value of n = 0.386 being less than 1 indicates a negative cooperativity in the binding of thrombin to the GFET biosensor that may be due to the protein–protein interactions upon binding or increased charge carrier scattering with increased ligand binding.[4,59] The best fit value of K_D = 375.8 ± 165.6 pM is in the similar range as reported previously.[44,61] Based on the obtained calibration curve, the calculated limit of detection (LOD) of our sensor is 2.6 pM (see the ESI† for details).

4.2.3 Selectivity of the GFET biosensor. The selectivity of the biosensor was tested against another common protein biomarker lysozyme. For this experiment, the GFET device functionalized with thrombin-binding aptamer was exposed to various concentrations (1, 10, 100, and 1000 nM) of lysozyme in 0.01× PBS buffer through the microchannel and incubated for 45 minutes. The measured I_D–V_{GS} characteristic curves are presented in Fig. 4C which shows the ability of the device to
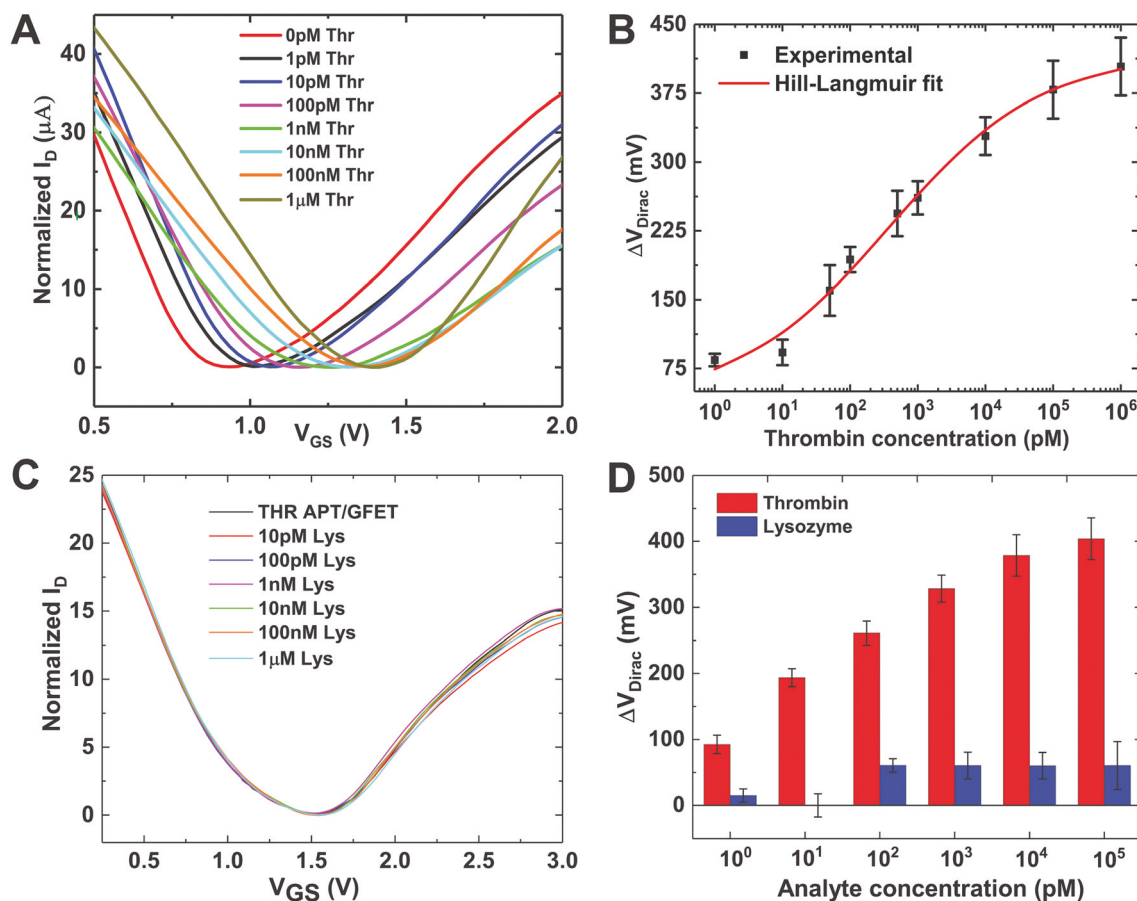
Fig. 4 Performance of the microfluidic-integrated GFET biosensor: (A) I_D–V_{GS} transfer characteristics of the GFET biosensor after exposure to different concentrations of thrombin protein; (B) concentration dependent calibration curve of the biosensor and its Hill–Langmuir fit (R^2 = 99.25%). The sample set is n = 3 and the error bar represents 1 standard error; (C) I_D–V_{GS} transfer characteristics of the GFET thrombin biosensor after exposure to different concentrations of lysozyme protein; and (D) comparative bar chart showing the ΔV_{Dirac} of the GFET thrombin sensor after exposure to different concentration of thrombin and lysozyme protein.

Table 1 Summary of the Hill–Langmuir fitting parameters of the voltage calibration curve

Hill–Langmuir parameters	Value	Error
V_0	39.2 mV	±30.6 mV
V_m	418.2 mV	±20.8 mV
K_D	375.8 pM	±165.6 pM
n	0.386	±0.081

screen out non-specific binding or unwanted adsorption on the surface of GFET. A comparative bar chart showing the Dirac voltage shift for both thrombin and lysozyme is shown in Fig. 4D. Exposure to high concentrations of lysozyme does cause some degree of Dirac voltage shift possibly due to the protein either nonspecifically binding to the anti-thrombin aptamer or directly adsorbing to the graphene surface. In either case, the positively charged lysozyme[62] affects the doping level of the GFET (i.e. p-type doping) in the same way the thrombin does to the device. However, its effect is relatively

small compared to that of thrombin of the same concentration, as shown in the chart.

4.2.4 Real-time and transient measurements. The transient FET measurements were performed on the device to monitor the protein–aptamer interaction in real-time. Various concentrations (0 pM–1 μM) of thrombin in 0.01× PBS were added to the sensor for 1 hour. To check the selectivity of the sensor, the GFET was also tested against a high concentration (1 μM) of lysozyme for the same amount of time period. The signal $I_D(t)$ was recorded while keeping V_{GS} and V_{DS} constant. The time-dependent measurements are shown in Fig. 5A. A gradually drifting background signal has been subtracted from $I_D(t)$. It can be seen that for each concentration of thrombin exposure, $I_D(t)$ follows an exponentially decreasing profile until PBS washing buffer was introduced to dissociate and remove the bound thrombin. The figure also shows that there is minimal change in I_D when exposed to lysozyme. Fig. 5B shows the enlarged view of the association and dissociation curves for the 1 μM thrombin concentration. After analyte injection into the microfluidic device, it took approximately
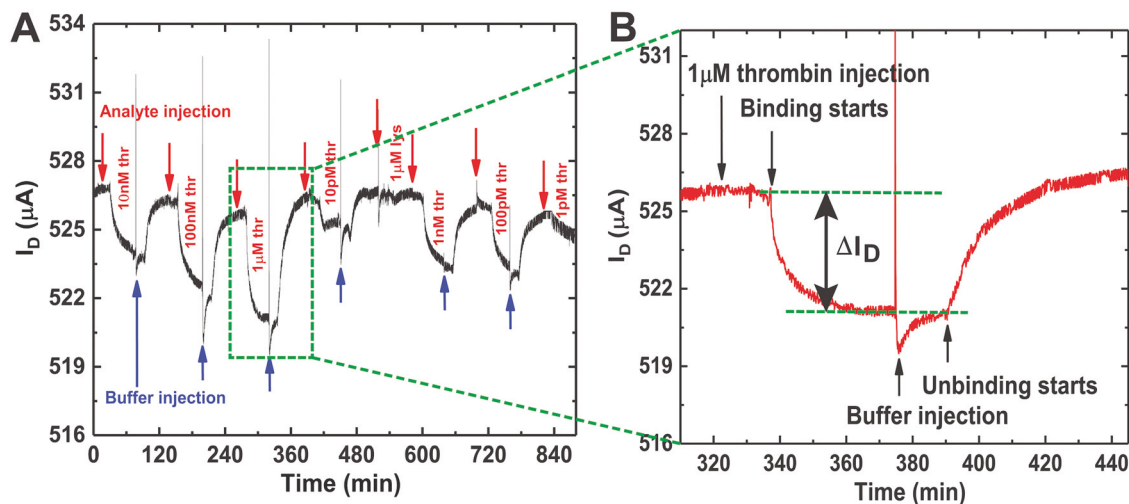
Fig. 5 (A) The continuous real-time measurements of the GFET biosensor. The plot depicts the transient measurement of the microfluidic-integrated GFET module biosensor. The liquid gate was fixed at V_{GS} = 0.75 V while the drain–source voltage was maintained at V_{DS} = 1.0 V. A constant flow rate of 20 μl min^{-1} was maintained throughout the experiment. Data points were collected every 1 second. A baseline drift of 9.378 nA min^{-1} has been subtracted from the curve. Sharp spikes around the introduction of thrombin and the PBS buffer are noises associated with switching of the syringes; and (B) binding and unbinding process for the thrombin with concentration of 1 μM.

15 minutes for $I_D(t)$ to respond due to the time required for the liquid to reach the GFET. As soon as the analyte reaches the sensor, target binding occurs and the signal drops exponentially until it reaches a steady-state approximately after 35 minutes. The amount of drop (ΔI_D) in the drain–source current is plotted against the thrombin concentrations resulting in the current calibration curve in Fig. S3† that clearly indicates the concentration-dependent binding between the aptamer and the protein. Table S2† summarizes the best fit $(R^2 = 0.9778)$ values of the Hill–Langmuir fitting parameters of the current calibration curve. The corresponding dissociation constant is found to be K_D = 731.7 pM which is comparable to the value obtained from the voltage calibration curve.

The selectivity of the sensor towards thrombin was again confirmed from this experiment as introducing 1 μM lysozyme did not cause any significant change to the $I_D(t)$ signal. The sensor can also be regenerated by simply rinsing with PBS buffer which has been confirmed by the unbinding process and the baseline curve returning to the initial value to approximately 525 μA shown in Fig. 5B.

When recording the $I_D(t)$ measurement, the raw data exhibits a gradual upward drift over time. This slow increase in the baseline current can be explained by the possible dissociation of pyrene anchors from the graphene surface resulting in a loss of aptamers from the GFET.[44] This loss of aptamers, although small in quantity, could shift the Dirac point in a positive direction causing $I_D(t)$ to rise (decrease of n-type doping) over time. However, this drift can be modeled using the formula: $g_m = \frac{\Delta I_D}{\Delta V_{GS}}$ (see the ESI† for details). In our devices, the measured baseline drift was ΔI_D = 9.378 nA min^{-1} which corresponds to a ΔV_{GS} changing at a rate of 202 μV min^{-1}. At this rate, 50% of the aptamer coating would dis-

sociate after approximately 10 hours (*i.e.* the time required to shift ΔV_{GS} = 117 mV) which is almost close to the previously reported value.[44] The measurements in Fig. 5 are the result after baseline correction by subtracting the current drift.

5 Conclusions

In conclusion, in this work, we have developed a microfluidic-integrated miniaturized GFET biosensor module for selective detection of thrombin biomarker. Thrombin is often used as a model protein in protein biosensing. It is also known for its several biomedical significances such as its critical role in hemostasis and thrombosis, involvement in several cardiovascular diseases and regulation of tumor growth. The binding affinity of the protein–aptamer interaction was quantified with a dissociation constant value of 375.8 pM which was further confirmed by real-time thrombin detection measurements under the continuous flow-through mode. In contrast to the measurements under static fluid (stopped flow) which can potentially be susceptible to mass transfer-limited kinetic binding process, the continuous flow-through strategy can improve the accuracy of the measurements for determining the aptamer–protein binding kinetics by promoting mass transfer in the fluidic channel. We also characterized the functionalization of aptamers on the GFET surface by Raman, UV-Vis and FTIR spectroscopy techniques. The sensor is able to detect thrombin as low as 2.6 pM. For future work, testing our devices with real physiological samples such as saliva, urine, or serum will further validate our biosensing platform as a potential point-of-care diagnostic device. Furthermore, achieving the clinically relevant detection limit and sensitivity

from these sample fluids will demonstrate the prospect of real-world use of this technology.

Conflicts of interest

There are no conflicts to declare.

Acknowledgements

References

1 A. K. Geim and K. S. Novoselov, *Nat. Mater.*, 2007, **6**, 183–191.

2 C.-H. Liu, Y.-C. Chang, T. B. Norris and Z. Zhong, *Nat. Nanotechnol.*, 2014, **9**, 273–278.

3 S. Mao, K. Yu, G. Lu and J. Chen, *Nano Res.*, 2011, **4**, 921.

4 J. Ping, R. Vishnubhotla, A. Vrudhula and A. T. C. Johnson, *ACS Nano*, 2016, **10**, 8700–8704.

5 E. Stolyarova, K. T. Rim, S. Ryu, J. Maultzsch, P. Kim, L. E. Brus, T. F. Heinz, M. S. Hybertsen and G. W. Flynn, *Proc. Natl. Acad. Sci. U. S. A.*, 2007, **104**, 9209–9212.

6 X. Tang, H. Zhang, X. Tang and K. W. C. Lai, *Mater. Res. Express*, 2016, **3**, 076203.

7 P. T. Yin, S. Shah, M. Chhowalla and K.-B. Lee, *Chem. Rev.*, 2015, **115**, 2483–2531.

8 D. Yu and L. Dai, *J. Phys. Chem. Lett.*, 2010, **1**, 467–470.

9 S. Ghosh, N. I. Khan, J. G. Tsavalas and E. Song, *Front. Bioeng. Biotechnol.*, 2018, **6**, 29.

10 N. I. Khan, A. G. Maddaus and E. Song, *Biosensors*, 2018, **8**(1), 7.

11 G. Liang, Y. Man, X. Jin, L. Pan and X. Liu, *Anal. Chim. Acta*, 2016, **936**, 222–228.

12 F. Rohrbach, H. Karadeniz, A. Erdem, M. Famulok and G. Mayer, *Anal. Biochem.*, 2012, **421**, 454–459.

13 M. Kokkonen, M. Jestoi and A. Rizzo, *Food Addit. Contam.*, 2005, **22**, 449–456.

14 M. Liss, B. Petersen, H. Wolf and E. Prohaska, *Anal. Chem.*, 2002, **74**, 4488–4495.

15 M. Minunni, S. Tombelli, A. Gullotto, E. Luzi and M. Mascini, *Biosens. Bioelectron.*, 2004, **20**, 1149–1156.

16 C. Nakamura, T. Kobayashi, M. Miyake, M. Shirai and J. Miyakea, *Mol. Cryst. Liq. Cryst. Sci. Technol., Sect. A*, 2001, **371**, 369–374.

17 W. U. Dittmer, A. Reuter and F. C. Simmel, *Angew. Chem., Int. Ed.*, 2004, **43**, 3550–3553.

18 T. G. McCauley, N. Hamaguchi and M. Stanton, *Anal. Biochem.*, 2003, **319**, 244–250.

19 S. Hideshima, R. Sato, S. Kuroiwa and T. Osaka, *Biosens. Bioelectron.*, 2011, **26**, 2419–2425.

20 D. Niwa, K. Omichi, N. Motohashi, T. Homma and T. Osaka, *Sens. Actuators, B*, 2005, **108**, 721–726.

21 J. Wang, K. Ito, T. Nakanishi, S. Kuroiwa and T. Osaka, *Chem. Lett.*, 2009, **38**, 376–377.

22 Z. Hao, Y. Zhu, X. Wang, P. G. Rotti, C. DiMarco, S. R. Tyler, X. Zhao, J. F. Engelhardt, J. Hone and Q. Lin, *ACS Appl. Mater. Interfaces*, 2017, **9**, 27504–27511.

23 S. Mao, J. Chang, H. Pu, G. Lu, Q. He, H. Zhang and J. Chen, *Chem. Soc. Rev.*, 2017, **46**, 6872–6904.

24 X. Dong, Y. Shi, W. Huang, P. Chen and L.-J. Li, *Adv. Mater.*, 2010, **22**, 1649–1653.

25 C.-T. Lin, P. T. K. Loan, T.-Y. Chen, K.-K. Liu, C.-H. Chen, K.-H. Wei and L.-J. Li, *Adv. Funct. Mater.*, 2013, **23**, 2301–2307.

26 H. Pinto and A. Markevich, *Beilstein J. Nanotechnol.*, 2014, **5**, 1842–1848.

27 X. Chen, Y. Liu, X. Fang, Z. Li, H. Pu, J. Chang, J. Chen and S. Mao, *Biosens. Bioelectron.*, 2019, **126**, 664–671.

28 S. Islam, S. Shukla, V. K. Bajpai, Y.-K. Han, Y. S. Huh, A. Ghosh and S. Gandhi, *Sci. Rep.*, 2019, **9**, 276.

29 Y. Ohno, K. Maehashi and K. Matsumoto, *J. Am. Chem. Soc.*, 2010, **132**, 18012–18013.

30 G. Wu, Z. Dai, X. Tang, Z. Lin, P. K. Lo, M. Meyyappan and K. W. C. Lai, *Adv. Healthcare Mater.*, 2017, **6**, 1700736.

31 S. Xu, J. Zhan, B. Man, S. Jiang, W. Yue, S. Gao, C. Guo, H. Liu, Z. Li, J. Wang and Y. Zhou, *Nat. Commun.*, 2017, **8**, 14902.

32 M. T. Stubbs and W. Bode, *Thromb. Res.*, 1993, **69**, 1–58.

33 W. Berg, B. Hillvärn, H. Arwin, M. Stenberg and I. Lundström, *Thromb. Haemostasis*, 1979, **42**, 972–982.

34 C. C. Heuck, U. Schiele, D. Horn, D. Fronda and E. Ritz, *J. Biol. Chem.*, 1985, **260**, 4598–4603.

35 S. Song, L. Wang, J. Li, C. Fan and J. Zhao, *TrAC, Trends Anal. Chem.*, 2008, **27**, 108–117.

36 S. Afsahi, M. B. Lerner, J. M. Goldstein, J. Lee, X. Tang, D. A. Bagarozzi, D. Pan, L. Locascio, A. Walker, F. Barron and B. R. Goldsmith, *Biosens. Bioelectron.*, 2018, **100**, 85–88.

37 L. Zuccaro, C. Tesauro, T. Kurkina, P. Fiorani, H. K. Yu, B. R. Knudsen, K. Kern, A. Desideri and K. Balasubramanian, *ACS Nano*, 2015, **9**, 11166–11176.

38 J. E. Schiel and D. S. Hage, *J. Sep. Sci.*, 2009, **32**, 1507–1522.

39 D. J. Beebe, G. A. Mensing and G. M. Walker, *Annu. Rev. Biomed. Eng.*, 2002, **4**, 261–286.

40 Y. Jiang, S. Zou and X. Cao, *Anal. Methods*, 2016, **8**, 6668–6681.

41 E. K. Sackmann, A. L. Fulton and D. J. Beebe, *Nature*, 2014, **507**, 181–189.

42 X. Wang, Z. Hao, T. R. Olsen, W. Zhang and Q. Lin, *Nanoscale*, 2019, **11**, 12573–12581.

43 J. Yang, C. Wang, Y. Zhu, G. Liu and Q. Lin, 2015 28th IEEE International Conference on Micro Electro Mechanical Systems (MEMS), 2015, pp. 569–572.

44 G. Saltzgaber, P. M. Wojcik, T. Sharf, M. R. Leyden, J. L. Wardini, C. A. Heist, A. A. Adenuga, V. T. Remcho and E. D. Minot, *Nanotechnology*, 2013, **24**, 355502.

45 G. Shen, H. Zhang, C. Yang, Q. Yang and Y. Tang, *Anal. Chem.*, 2017, **89**, 548–551.

46 X. Li, W. Cai, J. An, S. Kim, J. Nah, D. Yang, R. Piner, A. Velamakanni, I. Jung, E. Tutuc, S. K. Banerjee, L. Colombo and R. S. Ruoff, *Science*, 2009, **324**, 1312–1314.

47 H. Cho, B. R. Baker, S. Wachsmann-Hogiu, C. V. Pagba, T. A. Laurence, S. M. Lane, L. P. Lee and J. B.-H. Tok, *Nano Lett.*, 2008, **8**, 4386–4390.

48 L.-D. Li, H.-T. Zhao, Z.-B. Chen, X.-J. Mu and L. Guo, *Sens. Actuators, B*, 2011, **157**, 189–194.

49 J. Cox and A. D. Ellington, *Bioorg. Med. Chem.*, 2001, **9**, 2525–2531.

50 C.-H. Chu, I. Sarangadharan, A. Regmi, Y.-W. Chen, C.-P. Hsu, W.-H. Chang, G.-Y. Lee, J.-I. Chyi, C.-C. Chen, S.-C. Shiesh, G.-B. Lee and Y.-L. Wang, *Sci. Rep.*, 2017, **7**, 1–15.

51 N.-V. Nguyen, C.-H. Yang, C.-J. Liu, C.-H. Kuo, D.-C. Wu and C.-P. Jen, *Biosensors*, 2018, **8**, 98.

52 R. J. Chen, Y. Zhang, D. Wang and H. Dai, *J. Am. Chem. Soc.*, 2001, **123**, 3838–3839.

53 W. Yue, C. Tang, C. Wang, C. Bai, S. Liu, X. Xie, H. Hua, Z. Zhang and D. Li, *RSC Adv.*, 2017, **7**, 44559–44567.

54 X. Wang, Y. Zhu, T. R. Olsen, N. Sun, W. Zhang, R. Pei and Q. Lin, 2016 IEEE 29th International Conference on Micro Electro Mechanical Systems (MEMS), 2016, pp. 286–289.

55 G. I. Dovbeshko, N. Y. Gridina, E. B. Kruglova and O. P. Pashchuk, *Talanta*, 2000, **53**, 233–246.

56 Y. Zhu, Y. Hao, E. A. Adogla, J. Yan, D. Li, K. Xu, Q. Wang, J. Hone and Q. Lin, *Nanoscale*, 2016, **8**, 5815–5819.

57 E.-L. Gui, L.-J. Li, P. S. Lee, A. Lohani, S. G. Mhaisalkar, Q. Cao, S. J. Kang, J. A. Rogers, N. C. Tansil and Z. Gao, *Appl. Phys. Lett.*, 2006, **89**, 232104.

58 R. Gesztelyi, J. Zsuga, A. Kemeny-Beke, B. Varga, B. Juhasz and A. Tosaki, *Arch. Hist. Exact Sci.*, 2012, **66**, 427–438.

59 M. B. Lerner, F. Matsunaga, G. H. Han, S. J. Hong, J. Xi, A. Crook, J. M. Perez-Aguilar, Y. W. Park, J. G. Saven, R. Liu and A. T. C. Johnson, *Nano Lett.*, 2014, **14**, 2709–2714.

60 J. N. Weiss, *FASEB J.*, 1997, **11**, 835–841.

61 X. Li, L. Shen, D. Zhang, H. Qi, Q. Gao, F. Ma and C. Zhang, *Biosens. Bioelectron.*, 2008, **23**, 1624–1630.

62 A. K. H. Cheng, B. Ge and H.-Z. Yu, *Anal. Chem.*, 2007, **79**, 5158–5164.